Light weighed: on the statistics and systematics of weak gravitational lensing

Smit, D.M.

Citation

Smit, D. M. (2021, December 8). *Light weighed: on the statistics and systematics of weak gravitational lensing*. Retrieved from https://hdl.handle.net/1887/3245825

1

Introduction

In his dialogue *Parmenides* (129B), Plato lets his master Socrates state:

> *"... nor, again, if a person were to show that all is one by partaking of one, and at the same time many by partaking of many, would that be very astonishing. But if he were to show me that the absolute one was many, or the absolute many one, I should be truly amazed."*

In Plato's Theory of Forms, it is argued that our empirical, sensible observations can only be of the many possible different reflections of an insensible, unique universal Form, an absolute and unchanging concept, outside the limits of our physical space-time.

If any branch of the natural sciences is restricted, in its quest for a truthful description of reality, by the glimpses granted by the Universe, it is astronomy. Astronomers may improve their instruments and statistical techniques, but cannot set up a controlled experiment on most celestial objects, change their position in our Milky Way or follow the billion year evolution of a singular object beyond 'momentary' observations lasting mere centuries or decades. In Plato's well known metaphor, we can only see the shadows on the wall of the cave and hope to discover the true reality outside it.

Plato's contemplations were of a metaphysical nature, and the comparison with astronomy would end here, but it should be noted that it is no coincidence that astronomy was part of the *quadrivium*, four arts (the other three being arithmetic, geometry, and music) required for admittance to his *Akademia*.

This thesis modestly attempts to combine scientific research, by which we mean the aforementioned description of our universe, with theoretical considerations of the statistical methods used for that research, or how we can derive that description from the reflections that we see. In this work, we focus on the matter distribution in groups and clusters of galaxies, and consider the intricacies of the method of weak gravitational lensing that we use, respectively.

This introduction starts with a conceptual overview in section 1.1, after which we give a more mathematical and technical summary of these subjects in section 1.2. Section 1.3 then gives a short outline of the scientific chapters.

1.1   Now you see me...

Astronomy is one of the oldest natural sciences. The mysteries of the night sky have captured the imaginations of ancient civilizations since prehistoric times[1].

One of the oldest stories of observations and interpretations is that of the Pleiades, "Seven Sisters" in Greek mythology, an open star cluster designated as M45, which may have inspired humans for 100,000 years (Norris & Norris 2021). The cluster consists of more than 1000 confirmed members, of which formally[2] ten can be seen by the naked eye (Kyselka 1993, Norris & Norris 2021), but in practice, only six[3] are visible to most people with good visual acuity in a dark night. Examples are Galileo's depiction of the Pleiades in his *Sidereus Nuncius* (1610), where he indicates six visible stars among 36 observable through his telescope, and the Greek Aratus of Soli in the third century BC, who reported that "only six [sisters] are visible to the eyes" (Krupp 1991). In Greek mythology, this is explained by one of the sisters (Merope) hiding from their pursuer Orion, the hunter. It is very likely that the cluster was observed and named, before the story was associated with it (Hard 2004), so why tell a story about seven sisters, when only six are seen?

Might this be an example of *confirmation bias*, that is, an observer interpreting what is seen in a way that 'fits the story' best, thereby confirming preexisting theories or beliefs? Is this mythological story adjusted, so it could fit the observations? This explanation is contradicted by the strong similarity, suggesting a common origin, of stories on a "lost sister" or "daughter"[4] among many cultures around the globe, even those that had not been in contact for 100,000 years (e.g. Aboriginal Australian cultures predating European contact, Burnham 1978, Gibson 2017).

An alternative hypothesis is posed by Norris & Norris (2021), who calculate from data of the Hipparcos satellite (Van Leeuwen 2009) that, because of the proper motion of Pleione, that star was 100,000 years in the past 8.4 arcminutes away from the much brighter Atlas, an angular distance that is more than a quarter or a full moon. Nowadays, the two are so close, that the glare from Atlas prevents Pleione from being seen by the naked eye under most circumstances.

If this hypothesis is true, then there is no mystery to the story of a "lost sister". That 'mystery' is supposed by us, because the cultural stories surrounding M45 do not match *our* observations, but they matched observations at the time the *root story* might have originated in Africa. This would mean that such an *observer's bias* would be ours.

1.1.1   Observations and bias

This thesis focuses on systematic effects, statistics and subsequent interpretation. In the context of the latter, we have already used the terms *confirmation bias*, a predisposition to prior beliefs, and *observer's bias*, an indication of limitations in the available information or perspective, and therefore categorized under *information bias*. In our interpretation of the general term, a bias is a discrepancy between an observation or interpretation, and the 'truth'.

---

[1]At least, that is our current *interpretation* of some artifacts, sites and their orientations.

[2]Using a criterion of an apparent 'visual magnitude' brighter than six ($m_V < 6$).

[3]In fact, the *Greek* interpretation includes Atlas, the father of the sisters, among those six, reducing the number of visible sisters to five in that cultural version.

[4]Or occasionally indeed two.

Every student has heard of the Copernican Revolution, the changing of our view of the universe from geocentric, revolving around Earth, to heliocentric, revolving around the Sun. The Ptolemaic geocentric model, in basis a set of circles with the Earth as center, upon which moved the Sun and planets, had known problems in its description of reality. Some of these, the observed change of speed and retrograde motions of objects such as planets, where the direction of motion on the sky seems to reverse, could not be explained without adding adjustments that compromised the philosophical elegance of the basic system. See Figure 1.1.

One such an adjustment was the addition of epicycles, little circles that themselves moved over the larger, basis circles. Another was the introduction of equants, extra points beside Earth, around which objects moved at constant angular speed, while moving around other points, the deferents, with constant distance (i.e. circles).
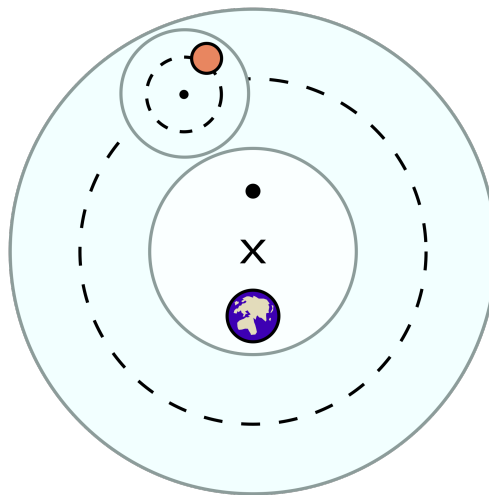

Figure 1.1: Representation of a planetary motion in the Ptolemaic geocentric model. The planet moves in a small epicycle. The center of that epicycle, shown as a small dot ·, moves in turn in a circle around the deferent, shown as ×, and with constant angular speed around the equant, shown as a bullet •. This image has been acquired in the public domain.

Copernicus presented the heliocentric model in 1543 as a mathematically much more elegant model and a better description of reality, explaining for instance retrograde motion as a natural consequence of the Earth's motion. However, an empirical model needs not only describe observations, but also predict them, and a major source of criticism for Copernicus's model was the need of many more epicycles to match new observations. The reason for this was the continued use of circles as a basis model. It was not until Kepler's laws of planetary motions in 1609, that circular orbits where replaced by elliptical ones, removing the need for epicycles and equants altogether.

As such, Copernicus's original heliocentric model is one of the most famous examples of *model bias*, a discrepancy that arises because the model is intrinsically not suited to describe the situation. Model bias is a recurring point of interest throughout this work. In chapter 2, we assess the assumption that we can model groups of galaxies that lie close to each other as separate objects, ignoring the influence they have on each other. In chapters 2, 3, and 5,

we discuss how we can model the center of groups of galaxies, as mis-centering can have a severe impact on our results.

In astronomy, one of the best known biases is the Malmquist bias, the fact that intrinsically brighter objects are easier to detect and therefore can be seen to a greater distance (Malmquist 1925). Looking back through our Universe, greater distance also means earlier times, so the Malmquist bias can create a false impression of evolution. If one doesn't account for this effect, the sample is said to suffer from *selection bias*. We consider a variant of this effect in chapter 2, where we estimate how many observed sources in the background of a supergroup of galaxies might actually be faint, instead of far away, and belong to the structure, throwing off our calculations.

In chapter 4 and 5, we discuss *statistical bias*, where it is not limitations in information or physical models that causes a biased result, but our *interpretation* of calculations. A *statistic* is nothing more than the result of an algorithm, usually a calculation, performed on a sample of values. The arithmetic mean is the best known example. We then interpret the meaning of this result. This a form of descriptive statistics, that aims to describe features of a population or a sample of that population, such as an 'average value' that best represents the sample.

As a well known example, when discussing salaries of the 'average' working citizen in a country, we have to take into account that there is a strict minimum wage (even if that minimum is zero), but not a maximum, with executives of large concerns or soccer players earning millions or even tens of millions. When the average income of a country is discussed, the median income is much more descriptive of the population and the mean can give a seriously biased interpretation of the people's prosperity.

The calculations performed are correct in themselves. The results just don't give an accurate description of reality. In chapters 4 and 5, we compare several descriptive statistics, or *estimators*, on samples of galaxy ellipticities. While these methods are all mathematically correct, they may not be equally appropriate to be used in a description of the matter distribution.

1.1.2 Dark matter

Astronomy studies many objects that cannot be observed directly, not even with a telescope, or not yet. The dark patches one sees when looking at the band of the Milky Way at night, known as The Great Rift, used to be thought of as emptiness, until observations (Barnard 1906) proved that they were actually obscuring dust clouds, that can nowadays be observed directly in infrared. In contrast, black holes, by their nature, can never be observed directly[5], only indirectly by energetic phenomena just outside their event horizon.

Before this century, planets outside our solar system were too small to be observed directly, until the observation of Fomalhaut b (Kalas et al. 2008) by the Hubble Space Telescope (HST). Before that, their existence could be deduced indirectly, e.g. from the regular dimming of the star they orbit when they pass in front of it, or the 'wobble' in the star's motion from their gravitational interaction. This requires the exoplanet to be sufficiently large or massive and our view of its orbit to be more or less from the side. This biased early samples of exoplanet candidates to massive planets, orbiting their star very closely.

In the same manner, one of the biggest mysteries in the universe to date (and a major subject of this thesis) was discovered: *dark matter*. The first indication of unseen matter came

---

[5]Which is why they are often called black hole *candidates*, as their nature cannot be confirmed by direct imaging.

from observations of stellar motions in our own Milky Way, from which Lord Kelvin deduced in 1884 that there must be many more stars than could be seen, so that "many of our supposed thousand million stars, perhaps a great majority of them, may be dark bodies" (Kelvin 1904). Kapteyn (1922) first coined the term "dark matter" to explain the distribution of stars and velocities, as seen from the solar neighborhood. Although it is sometimes mentioned that the work of Oort (1932) confirmed the hypothesis of Kapteyn, it was shown that these and similar works suffered from one or both of selection or model bias and that these works did not prove the need for dark matter (Kuijken & Gilmore 1989), but the concept was born.

Arguably the first real evidence for dark matter came from the work of Zwicky (1933), who studied the orbital motions of galaxies in the Coma cluster. Zwicky concluded from their large velocities that the visible mass, the known matter of stars, gas and dust, also known as *baryonic matter*, was not enough by a factor of more than 400 to keep them in place, instead of flying off. (Schwarzschild 1954) also found the mass-luminosity ration of the Coma cluster to be "bewilderingly high".

Freeman (1970) and Bosma (1981) found a similar effect when studying the rotation curves of spiral galaxies. If there was no mass beyond the disk, one would expect the rotational velocity to fall off the further one observed from the central mass distribution. However, the observed rotation curves remained flat far beyond the visible disks. Rubin (1983) made the connection to Zwicky's dark matter and discussed the implications for the geometry of the universe.

So far, the arguments for the existence of this unknown dark matter came from dynamical considerations. A next fundamental discovery came from observations of the Cosmic Microwave Background (CMB), first observed by Penzias & Wilson (1965) and mapped by the COBE satellite (Mather 1982). The CMB can be thought of as an afterglow of the Big Bang, created when the hot ionized plasma in the universe cooled down sufficiently to recombine into the matter we see today. From observations by the WMAP satellite, Spergel et al. (2003) and Hinshaw et al. (2007) showed that of the total matter in the universe, less than 20% was in the forms of baryons, and the rest was dark matter.

In fact baryonic and dark matter together only provide $\sim 30\%$ of the matter-energy content of the universe, while $\sim 70\%$ of the content of the universe is energy[6]. In this thesis, we use cosmological values consistent with results from the Planck satellite (Planck Collaboration et al. 2014), with 4.9% ordinary matter, 26.6% dark matter and 68.5% energy. So far, the nature of and observations of dark matter elude us, as elementary particle physics have no conclusive theoretical explanation and our instruments have not yet been able to detect it. We know it's there and we know it interacts through gravity, but so far there doesn't seem to be any interaction with electromagnetic radiation or baryonic matter.

The curvature of space-time

As dark matter can only be observed indirectly by its gravitational interactions, it follows that we rely on indirect methods to study the total distribution of all matter. Our method to study this distribution makes use of gravitational lensing, an effect of the curvature of spacetime, most accurately[7] predicted by Einstein's theory of general relativity (e.g. Eddington 1920,

---

[6]In fact, the nature of this energy is also 'dark', i.e. unknown and unobserved, possibly in the form of a cosmological constant Λ, a term first used by Einstein (1917)

[7]Classical theory, already by Newton in 1704, also predicts the bending of light rays, but is off by 50%.
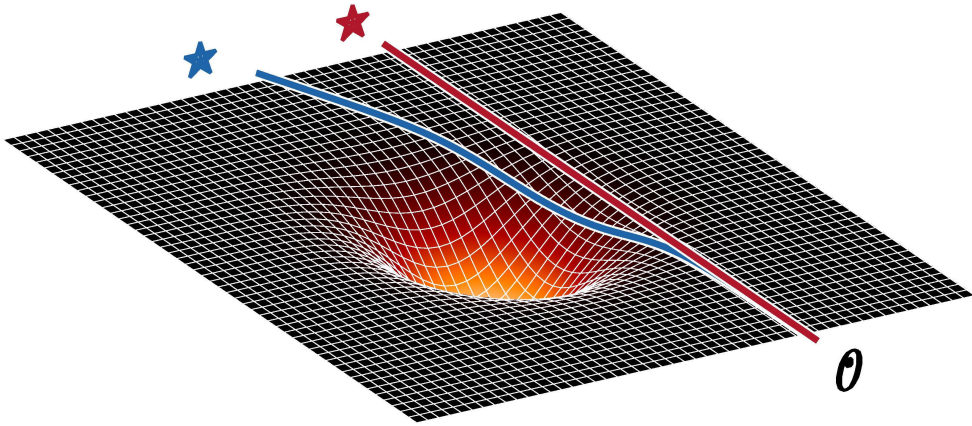
Figure 1.2: The curvature of spacetime causes the light rays from a source in the background (blue) to deflect from a straight line. An observer perceives an image (red) displaced from the position of the source.

Chwolson 1924).

In the general relativistic description, the geometry of spacetime is determined by the presence and state of energy and matter. More simply put, spacetime is bent due to a concentration of mass, an effect that we experience as gravity. Because light rays travel along the shortest path available, this path is no longer straight in a curved geometry (see Fig. 1.2). This makes gravitational lensing a direct probe of the geometry of the universe and the distribution of *all* matter, without the need to make assumptions about the astrophysical or dynamical state of observed phenomena.

The first observations of gravitational lensing were made by Dyson et al. (1920), during the solar eclipse on the 29th of May, 1919. Around this time, it was discovered that our Milky Way was just one of hundreds of billions (Lauer et al. 2021) of galaxies, that form the building blocks of the universe (Slipher 1915, Curtis 1917). Zwicky (1937) suggested that galaxies would be massive enough[8] lenses to make this effect easier to observe, and numerous enough to be likely candidates to be lensed. Measurement of this variant, aptly called galaxy-galaxy lensing, was first attempted by Tyson et al. (1984) and finally detected by Brainerd et al. (1996).

This thesis focuses on lensing by more massive structures, like groups and clusters of galaxies, first detected by Tyson et al. (1990). Perhaps one of the most powerful examples of gravitational lensing as a way to probe the matter distribution independent of astrophysical assumptions is given by the bullet cluster (Clowe et al. 2006, see Fig. 1.3).

The bullet cluster system actually consists of two clusters of galaxies that have passed through each other, the smaller cluster moving at higher velocity to the right being considered the 'bullet'. The groups of galaxies of these clusters can pass collisionlessly through each other and appear unaffected, but the intracluster gas, where most of the known, baryonic mass in these clusters resides (Clowe et al. 2006), lags behind. Their reconstruction of the

---

[8]Typical luminosities of bright galaxies like our own Milky Way are 100 billion times the luminosity of the Sun, $L_\star \sim 10^{11} L_\odot$.
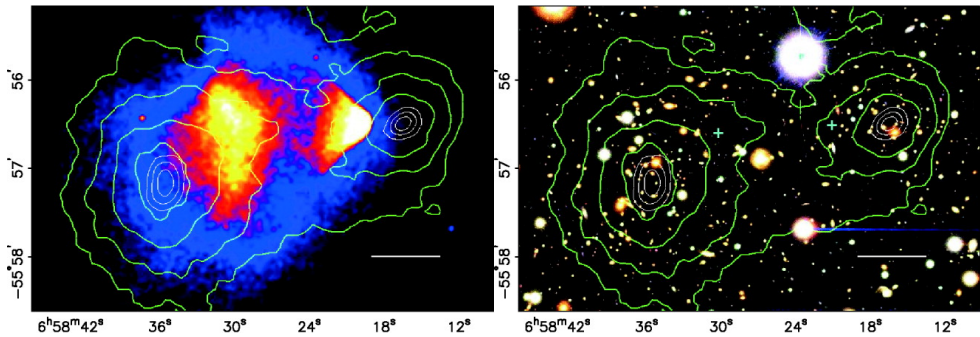
Figure 1.3: *Left.* A reconstruction of the matter distribution (green contours) using gravitational lensing compared to the X-ray emission of the hot gas (color scale), where most of the visible, baryonic matter of this system resides. *Right.* The same reconstruction, now compared to the location of the galaxies that make up the two subclusters. These images show that most of the total matter does not reside where most of the baryonic matter is observed, a clear indication that the major part is 'dark' and collisionless. Originally published in Clowe et al. (2006).

matter distribution using weak gravitational lensing clearly show that most of the total matter does not reside where most of the baryonic matter is observed, a clear indication that the major part is 'dark'.

1.2 Weak gravitational lensing

In this section, we introduce the mathematical framework of gravitational lensing, as well as the principles of weak lensing we have used in our work. We also present the central concepts to our statistical approach and our tests for systematic effects. We introduce terminology and notation conventions used in this thesis.

1.2.1 The basics of gravitational lensing

We start with an analytic derivation of the framework of weak lensing, the main observables and concepts that then form the basis for the research in this thesis. We refer the reader to excellent reviews such as Bartelmann & Schneider (2001), Schneider (2006), Hoekstra & Jain (2008), Bartelmann & Maturi (2017), for more in-depth approaches.

As the lensing effect is caused by rays of light being deflected by the curvature of space-time due to mass inhomogeneities along their path, we consider how a mass overdensity acts on the light rays from distant sources behind it. Figure 1.4 shows a simple representation of a gravitational lens system.

For the purposes of this work, the extent of the lensing mass along the line of sight, compared to the distances from observer to lens and from lens to background source, is negligible. In this so-called thin-lens approximation, we can describe the path of light by straight line segments. In this representation, we use angular-diameter distances D_l from observer to lens, D_{ls} from lens to background source[9], and D_s from observer to background

---

[9]More accurately, the distance to the source *plane* perpendicular to the line of sight from observer to lens, but in
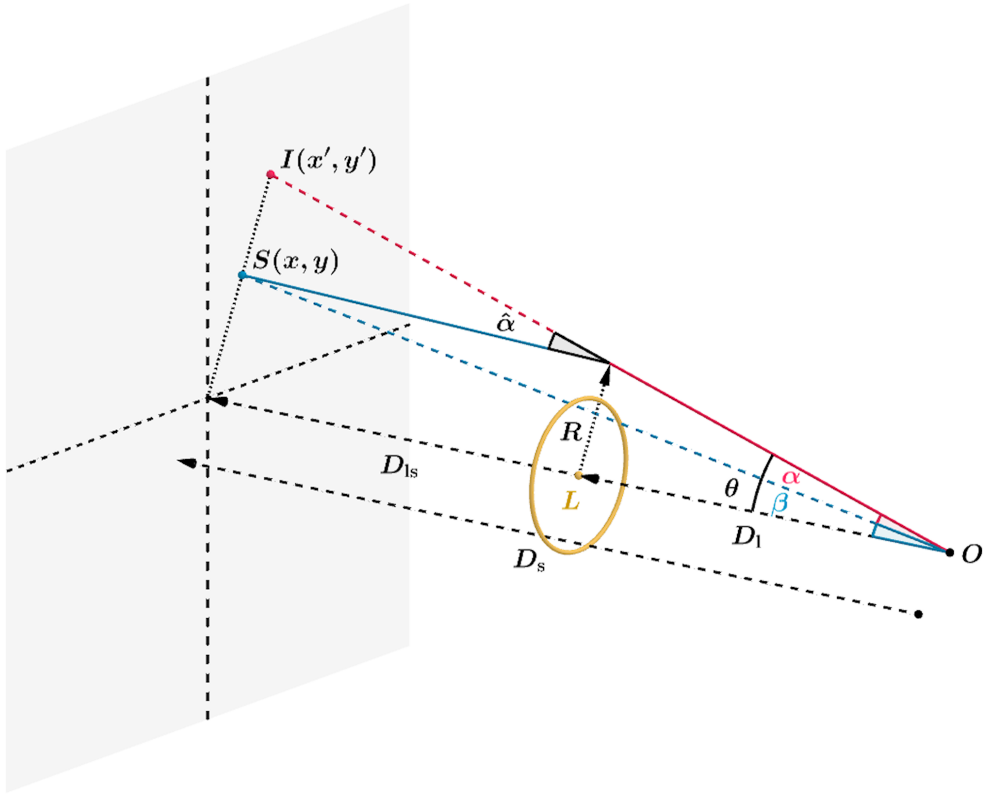
Figure 1.4: Representation of a gravitational lens system, showing the displacement of a source at position $S(x, y)$ to an image at position $I(x', y')$, where we take the origin of the source plane collinear with the positions of the lens L and the observer O. Based on Smit et al. (2021).

source.

The deflection angle $\hat{\vec{\alpha}}$ is determined by the gradient of the gravitational potential Φ perpendicular to the path of light, integrated along that path:

$$\hat{\vec{\alpha}} = -\frac{2}{c^2} \frac{1}{D_\mathrm{l}} \int \vec{\nabla}_\theta \Phi \, dl \,, \tag{1.1}$$

where $\vec{\nabla}_\theta$ is the two-dimensional gradient in angular coordinates perpendicular to the line of sight and the angular-diameter distance factor of D_l^{-1} arises from the conversion of physical to angular coordinates in the case of small angles.

This leads to an angular displacement, as seen from the observer and again using the small-angle approximation (see Fig. 1.4)

$$\vec{\alpha} = -\frac{D_\mathrm{ls}}{D_\mathrm{s}} \hat{\vec{\alpha}} \,, \tag{1.2}$$

---

this approximation, these are the same.

also called the reduced deflection angle, relating the observed position $\vec{\theta}$ of a distant point source to its unlensed position $\vec{\beta}$ by the lens equation

$$\vec{\beta} = \vec{\theta} - \vec{\alpha}. \tag{1.3}$$

Under the thin-lens approximation, the deflection of light rays by the lensing mass is then described by $\vec{\alpha} = \vec{\nabla}_\theta \psi$, where

$$\psi = \frac{2}{c^2} \frac{D_{ls}}{D_l D_s} \int \Phi \, dl \tag{1.4}$$

is the two-dimensional, dimensionless, lensing potential. In this way, the deflection angle can be related to the density of the lensing mass and to observable distortion of sources in the background, as follows, starting with the latter.

The differential effect of the deflection of light on the images $I(x, y)$ of background galaxies, which are extended sources, can to first order be described as a coordinate transformation, by taking the derivatives in the lens equation (1.3) of the original position β with respect to the observed position θ. Substituting $\vec{\nabla}_\theta \psi$ for $\vec{\alpha}$, we obtain the Jacobian of the lens mapping,

$$\begin{pmatrix} x' \\ y' \end{pmatrix} = \begin{pmatrix} 1 - \psi_{11} & -\psi_{12} \\ -\psi_{21} & 1 - \psi_{22} \end{pmatrix} \begin{pmatrix} x \\ y \end{pmatrix}, \tag{1.5}$$

with

$$\psi_{ij} = \frac{\partial^2 \psi}{\partial \theta_i \partial \theta_j}, \tag{1.6}$$

resulting in the lensed image $I(x', y')$, which is the key observable in our work.

Critical surface mass density and convergence

To interpret the effect on the source image, we note that the linear, symmetric coordinate transformation in eq. 1.5 can be decomposed in three parts, namely the identity I and two perturbations, consisting of an isotropic part describing a magnification, and an anisotropic, traceless part, describing a shearing of the image:

$$I - \frac{1}{2}(\psi_{11} + \psi_{22})I + \begin{pmatrix} -\frac{1}{2}(\psi_{11} - \psi_{22}) & -\psi_{12} \\ -\psi_{21} & \frac{1}{2}(\psi_{11} - \psi_{22}) \end{pmatrix} \tag{1.7}$$

To relate ψ_{ij} to the density of the lensing mass, we start with the isotropic term, which is half the Laplacian of the lensing potential: $\frac{1}{2}(\psi_{11} + \psi_{22}) = \frac{1}{2}\nabla_\theta^2 \psi$. Using equation 1.4 and the thin-lens approximation, introducing a factor of D_l^2 due to conversion between angular and physical coordinates, we obtain

$$\frac{1}{2}\nabla_\theta^2 \psi = \frac{1}{c^2} \frac{D_l D_{ls}}{D_s} \int 4\pi G\rho \, dl, \tag{1.8}$$

which is a dimensionless quantity. Defining the surface mass density as

$$\Sigma \equiv \int \rho \, dl \tag{1.9}$$

and gathering the remainder of the right-hand side into

$$\frac{4\pi G}{c^2} \frac{D_l D_{ls}}{D_s} \equiv \Sigma_{cr}^{-1} , \qquad (1.10)$$

with Σ_{cr} called the critical surface mass density, we find that the isotropic term can be written as

$$\kappa \equiv \frac{1}{2}\nabla_\theta^2 \psi = \frac{\Sigma}{\Sigma_{cr}} , \qquad (1.11)$$

where we recognize κ as a normalized dimensionless surface mass density. Recognizing that $\nabla_\theta^2 \psi = \vec{\nabla} \cdot \vec{\alpha}$ is the divergence of the deflection of the light rays, or the manner in which those light rays converge due to the lensing effect, κ is simply called the convergence.

Shear and intrinsic ellipticity

The shear matrix in eq. 1.7 has two independent components $\gamma_1 = \frac{1}{2}(\psi_{11} - \psi_{22})$ and $\gamma_2 = \psi_{12} = \psi_{21}$, with $\gamma \equiv \gamma_1 + i\gamma_2$ called the complex shear. Eq. 1.5 then becomes

$$\begin{pmatrix} x' \\ y' \end{pmatrix} = \begin{pmatrix} 1 - \kappa - \gamma_1 & -\gamma_2 \\ -\gamma_2 & 1 - \kappa + \gamma_1 \end{pmatrix} \begin{pmatrix} x \\ y \end{pmatrix}. \qquad (1.12)$$

This transformation leads to magnification and distortion of the light distribution of background sources. Weak lensing magnification analyses (e.g. Hildebrandt et al. 2009, Van Waerbeke et al. 2010, Hildebrandt et al. 2011) require the intrinsic (distribution of) source sizes or magnitudes. In weak shear analyses, the focus lies on the net distortion or reduced shear $g = g_1 + ig_2 \equiv (\gamma_1 + i\gamma_2)/(1 - \kappa)$:

$$\begin{pmatrix} x' \\ y' \end{pmatrix} = (1 - \kappa)\begin{pmatrix} 1 - g_1 & -g_2 \\ -g_2 & 1 + g_1 \end{pmatrix} \begin{pmatrix} x \\ y \end{pmatrix} , \qquad (1.13)$$

where the transformation is written as a multiplication of $(1 - \kappa)$ and a distortion matrix describing the alignment of lensed sources in the foreground potential.

The effect on a circular source is a shearing into an ellipse with axis ratio $q = \frac{b}{a}$, where

$$q = \frac{1 - |g|}{1 + |g|} \quad \Leftrightarrow \quad |g| = \frac{1 - q}{1 + q} = \frac{a - b}{a + b} , \qquad (1.14)$$

and position angle φ via

$$g = |g|(\cos 2\varphi + i\sin 2\varphi) . \qquad (1.15)$$

See Fig. 1.5.

This gravitational distortion cannot be measured directly in practice. Galaxies that are used as background sources, have an intrinsic shape distribution and we can only measure the combined effect of their intrinsic shape and a weak lensing distortion. While galaxies often have complex morphologies, it is adequate to describe images by their quadrupole brightness moments or their ellipticities, and their respective response to weak shear distortions. A common definition[10] of the shape of an image with elliptical isophotes is the ellipticity $\epsilon =$

---

[10] An alternative definition of ellipticity is often denoted as $|\chi| = \frac{1-q^2}{1+q^2}$, related to the geometrical eccentricity, and called polarization (e.g. Seitz & Schneider 1995, Viola et al. 2014, and section 1.2.2).
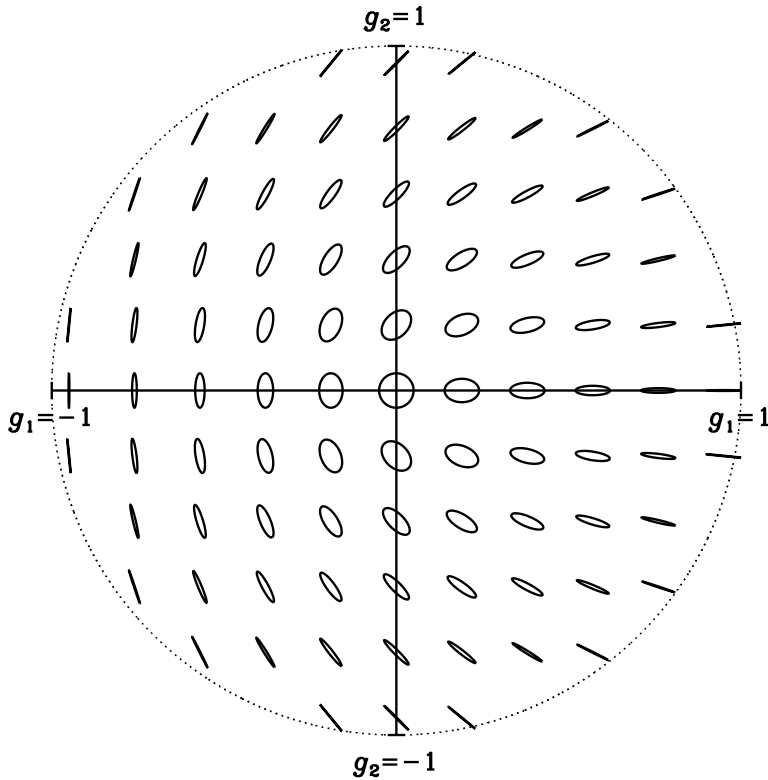
Figure 1.5: The effect of shear on an intrinsically round source. The g_1 component stretches the image horizontally or vertically. The g_2 component stretches the image diagonally.

$\epsilon_1 + i\epsilon_2$, defined as the reduced shear needed to create this image from an image with circular isophotes (Bernstein & Jarvis 2002, Kuijken 2006).

The complex notation gives a most straightforward formulation of the ellipticity ϵ that results after transforming an image with intrinsic ellipticity ϵ^I with a distortion g. As shown by Seitz & Schneider (1997),

$$\epsilon = \frac{\epsilon^I + g}{1 + g^*\epsilon^I} \quad \text{for} \quad |g| \leq 1 \,, \tag{1.16}$$

with g^* the complex conjugate of g.

The intrinsic shape distribution is called shape noise and assuming no preferred direction on the sky, should average to zero: $\langle \epsilon^I \rangle = 0$. Seitz & Schneider (1997) showed that, for eq. 1.16, the mean[11] $\langle \epsilon \rangle$ does not depend on the intrinsic shape distribution $P(\epsilon^I)$. Each background shape measurement ϵ is then an unbiased, albeit very noisy, estimate of the reduced shear g, but only in the absence of further sources of noise, that would alter the observed distribution of ϵ.

---

[11]Or, in fact, any n−th moment $\langle \epsilon \rangle^n$.

In practice, there are always sources of error that manifest as 'noise' in the observed ellipticity values, such as pixel noise of the detector, systematic distortions in the optical system and limitations in modeling algorithms.

1.2.2   The measurement of shapes

While the basis of weak gravitational lensing is given in analytic detail, in practice one has to deal with many systematic effects, when measuring the main observable, the shapes of background sources. As many of these effects depend on specific telescopes, instruments, pipelines and surveys, the most detailed and technical descriptions are given in the corresponding (series of) papers.

Here we aim to give the reader, as a frame of reference for this thesis, a qualitative overview of a selection of effects, that will be analyzed in more detail in chapters 2 and 3. For a more detailed treatise, we point the reader to the references given there and in the following sections.

Images and distortions

At the observer's end in the schematic of Fig. 1.4, the light rays pass through the atmosphere, in case of ground-based observations, and through the telescope optics, before being registered by the detector of the instrument. The response of this total optical 'system' to the received signal is called the point spread function (PSF), its Fourier transform being the optical transfer function. It describes the image of a point source.

The PSF causes a pattern of ellipticity distortions that varies over the field of view, and can be modeled using the images of stars (which are unresolved and can therefore be treated as point sources). The correction is then a deconvolution. This can be done on a single image, if there are enough stars in the field of view to properly sample the PSF pattern.

Observations which have relatively few stars, typically at high galactic latitude, can be corrected using dense stellar fields as reference. Hoekstra (2004) modeled the time-invariant spatial pattern of the PSF by averaging many fields. To properly take the temporal variations into account, a principal component analysis (PCA) can be used (e.g. Jarvis & Jain 2004, Schrabback et al. 2007, 2010). We employ this technique in the weak lensing analysis of imaging data taken with the Advanced Camera for Surveys (ACS) on the HST in chapter 2.

In this way, the term PSF is used as a catchall, and the resulting distortions are oftentimes corrected for in a similar fashion: a correction for the combined PSF pattern, without the need to identify individual causes. As pointed out by Jarvis et al. (2008), a physical model for a known contribution to the PSF may be more accurate than an average or a PCA derived from noisy data. In this context it is worth noting, that both Jarvis & Jain (2004) and Schrabback et al. (2007) interpret their first principal component to indicate telescope focus.

The turbulence of the atmosphere causes a blurring of the image called seeing. If exposure times are long enough, the direct effect on the ellipticity or the PSF is negligible (Heymans et al. 2012a). It is usually the dominant factor in the size of the PSF for ground based observations and therefore effectively sets the limit on the angular resolution of the observations, which in turn limits the number statistics of resolved background sources that can be used for lensing. To give some examples: the seeing of the Wide Field Imager (WFI) data used in chapter 3 varies between 0.75″ and 1.35″ with a median of 1.0″, whereas the

median seeing conditions for the Canada-France-Hawaii Lensing Survey (CFHTLenS, Heymans et al. 2012b) and the Kilo-Degree Survey (KiDS, de Jong et al. 2013) Data Release 3 (KiDS-450, de Jong et al. 2017) used in chapters 4 and 5 are 0.72″ (Erben et al. 2013) and 0.66″ (Hildebrandt et al. 2017), respectively.

Observations from space are not limited in resolution by seeing, but are diffraction-limited, the fundamental physical limit due to diffraction determined by the telescope aperture size and the wavelength observed. The resulting diffraction pattern makes the PSF more complex. An important type of artifact seen in space-based observations is caused by the deterioration of the instrument CCDs, due to constant exposure to cosmic rays, outside the protective atmosphere. This causes a charge-transfer inefficiency (CTI), leading to trails in the CCD readout direction. These trails will affect the measured PSF and shear patterns and need to be corrected for, as is done in e.g. Rhodes et al. (2007), Massey et al. (2010) and in chapter 2.

A final aspect we mention here concerns the translation from instrument (CCD) response to image. The dominant source of noise in the image is pixel noise, mainly due to sky background Poisson noise and CCD readout noise. This increases uncertainties in shape measurements and causes measurement bias in the derived shapes, as the dependence of ellipticity on pixel values is non-linear (see e.g. Refregier et al. 2012, Melchior & Viola 2012, Kacprzak et al. 2012).

Pixel noise can be compensated by increasing exposure time. As a CCD image is quantized on a rectangular grid, an observed field of view is built from a set of dithered exposures. The final image is obtained by stacking these exposures, thus obtaining a longer total exposure time and a higher signal-to-noise ratio. A disadvantage of using such a stacked image, is that the individual exposures have their own PSF patterns, which are then also stacked. Especially in areas of the final, stacked image that are not covered by all individual exposures, due to edges or gaps in the CCD mosaic, the resulting PSF pattern may be discontinuous[12]. We assess this effect in chapter 3. Shape measurement methods such as the *lens*fit pipeline presented in Miller et al. (2013) model the full set of single exposures instead.

Measurement and bias

Given the necessary control of systematics, and the fact that the modeling of these systematics and the intended source ellipticity measurements are based on noisy images, the development of accurate and robust shape measurement methods has been and still remains a major investment in the field of weak lensing (see e.g. Mandelbaum 2018). Community-driven projects, such as the Shear Testing Programme (STEP, Heymans et al. 2006, Massey et al. 2007), and the GRavitational lEnsing Accuracy Testing challenges (GREAT, Bridle et al. 2010, Kitching et al. 2012, Mandelbaum et al. 2015), have led to a decrease in measurement bias and variances and a better understanding of remaining systematic effects and biases.

In this thesis, we explore three particular methods, based on surface brightness moments or model fitting. In chapter 2 and 3, we make use of the KSB method (Kaiser et al. 1995). In chapter 3, we compare KSB and the Shapelets method (Refregier 2003, Refregier & Bacon 2003). In chapter 4 and 5, we make use of the shear catalogs of CFHTLenS and KiDS-450, both derived with *lens*fit (Miller et al. 2007, Kitching et al. 2008).

---

[12]This problem is confounded when the single exposure times become short enough for the atmosphere to contribute to the PSF ellipticity pattern.

KSB describes images by their second order brightness moments in angular coordinates

$$Q_{ij} = \frac{\int \theta_i \theta_j W(\theta) I(\theta) d^2\theta}{\int W(\theta) I(\theta) d^2\theta} \tag{1.17}$$

with I the surface brightness and W is a certain weight or window function. This gives three independent quadrupole moments, Q_{11}, Q_{22}, and $Q_{12} \equiv Q_{21}$. KSB determines the complex polarization

$$\chi = \chi_1 + i\chi_2 = \frac{Q_{11} - Q_{22} + 2iQ_{12}}{Q_{11} + Q_{22}}. \tag{1.18}$$

This polarization is related to the eccentricity and is clearly zero for a circular source. However, it differs from the definition of the ellipticity ϵ given in section 1.2.1, which can be defined in terms of the second order brightness moments as

$$\chi = \chi_1 + i\chi_2 = \frac{Q_{11} - Q_{22} + 2iQ_{12}}{Q_{11} + Q_{22} + 2\sqrt{Q_{11}Q_{22} - Q_{12}^2}}, \tag{1.19}$$

and the two definitions are related through

$$\chi = \frac{2\epsilon}{1 + |\epsilon|^2} \tag{1.20}$$

This means that $\langle\chi\rangle$ is a biased estimator of g, as it depends explicitly on the distribution of intrinsic shapes χ^I (Schneider & Seitz 1995). However, in the limit of weak shear, where $\kappa \ll 1$ and $\gamma \ll 1$, we have $\gamma \approx g \approx \langle\epsilon\rangle \approx \frac{1}{2}\langle\chi\rangle$. Besides this statistical bias, one has to consider the model[13] bias from approximations in the PSF correction and noise bias due to the non-linear combination of noisy estimates of Q_{ij}.

In the Shapelets formalism, the light distribution of a source is expanded in the orthonormal basis set of Gauss-Hermite functions. This allows for a flexible model and has the advantage that the behavior of these basis functions under simple transformations (such as an applied shear or smearing by a PSF) is well understood. A PSF model $\boldsymbol{P}$ can then be constructed from the shapelet expansions of bright stars in the image. In the implementation of Kuijken (2006), which we use in chapter 3, sources are described as intrinsically circular, with an expansion

$$\boldsymbol{C} \equiv c_0 C^0 + c_2 C^2 + c_4 C^4 + \dots, \tag{1.21}$$

with C^n circular shapelet basis functions (with n always even) and c_n free parameters. This circular model is then transformed by a distortion

$$\boldsymbol{D} \equiv 1 + \epsilon_1 \boldsymbol{S}_1 + \epsilon_2 \boldsymbol{S}_2 + \delta_1 \boldsymbol{T}_1 + \delta_2 \boldsymbol{T}_2, \tag{1.22}$$

where $\boldsymbol{S}_i$ and $\boldsymbol{T}_i$ are the first-order shear and translation operators, as given by Refregier & Bacon (2003). The free translation δ is needed to ensure an optimal centroid fitting. (We remind the reader that for a method using surface brightness moments, like KSB, the centroid is derived from the first order brightness moments.) This model is then convolved by the PSF model and the resulting model $\boldsymbol{M} = \boldsymbol{P} \cdot \boldsymbol{D} \cdot \boldsymbol{C}$ is then fitted to the observed sources.

---

[13]In this form also called method bias, see Viola et al. (2014).

This forward convolution with $\boldsymbol{P}$ is numerically more stable than deconvolving noisy source images and allows for a propagation of pixel noise, to ensure accurate uncertainty estimates σ_{ϵ_i}. Velander et al. (2011) showed the advantage of the shapelet flexibility, when measuring higher order distortions in diffraction limited HST images. Besides the noise bias due to fitting a (non-linear) model to noisy images, one has to consider model bias, as the shapelet basis functions are chosen for their elegant transformation properties, and are not realistic representations of galaxy shapes. This mismatch is diminished if one allows the expansion to go to higher order, but in reality the flexibility of the shapelets becomes a weakness, as we start fitting noise. In practice, we use a cutoff in the shapelet expansion, which in itself may introduce another (mild) model bias.

*Lens*fit is a Bayesian model-fitting method, using a galaxy model consisting of Sérsic (1963, 1968) bulge and disc components. Besides using the same or similar free parameters like the aforementioned methods, including the ellipticity ϵ, galaxy size and flux, and galaxy centroid, this pipeline also fits the ratio of bulge to disc, partly discriminating between late and early type galaxies (Miller et al. 2013, Fenech Conti et al. 2017). The log-likelihood (or goodness-of-fit) then has the form

$$\log \mathcal{L} = - \sum_i \frac{(y_i - S\,[f_\mathrm{B} b_i + (1 - f_\mathrm{B})d_i])^2}{2\sigma_i^2} \tag{1.23}$$

with S the galaxy flux, b_i and d_i the bulge and disc components and f_B the bulge fraction. It uses pixel-based models of the PSF, which allows for discontinuities between CCDs in the CCD mosaic and uses the full information of all single exposures containing the source. The posterior likelihood is then marginalized over the parameters that are not of interest, using assumed prior distributions, leaving a likelihood surface as function of ϵ_1 and ϵ_2. The aim is to alleviate possible model bias by using an adequate set of priors for the parameters to be marginalized over. To avoid a poorly constrained likelihood, in particular a cutoff in the ellipticity is needed, $\epsilon_\mathrm{max} = 0.804$ for CFHTLenS (Miller et al. 2013) and $\epsilon \approx 1$ for KiDS-450 (Fenech Conti et al. 2017), which introduces a bias due to truncation that needs to be calibrated and can lead to visible signatures that affect the most elliptical ϵ (e.g. Smit & Kuijken 2018, chapter 4).

In conclusion, each pipeline has its own strengths and biases, that are addressed per individual cause, just as is recommended by Jarvis et al. (2008) for the modeling of the PSF. The remaining discrepancies with the 'true' reduced shear g, are modeled as a similar catchall, first order approximation $\epsilon_\mathrm{est} = (1 + m)\epsilon_\mathrm{true} + c$, with ϵ_est the estimated ellipticity, c a constant additive bias, and m a multiplicative measurement bias. c may in general be readily corrected for, if it's not position dependent, which is most likely the result of an undersampled PSF (Van Uitert & Schneider 2016). Usually, m is determined using simulations and is dependent on observed properties, such as source brightness and size. These correlations are weak, making estimates of m on a source-by-source basis very noisy. The correction is then done on a sample basis. For instance, if source weights for the measured ellipticities, based on the estimated uncertainties by the pipeline, are w_i and the estimated multiplicative biases are m_i, one generally corrects the estimated lensing signal by a factor $(1 + K)^{-1}$, with K of the form

$$K = \frac{\sum_i w_i m_i}{\sum_i w_i}, \tag{1.24}$$

using the same sample of sources (e.g. Viola et al. 2015, Dvornik et al. 2017).

1.2.3   The inference of weak shear

Given a catalog of robust, reliable shapes ϵ_i, the final measured distribution $P(\epsilon_i)$ is modified from the theoretical form $P(\epsilon)$ (eq. 1.16), due to measurement noise, even if the individual measurements are unbiased. At this point, it is instructive to review our definition of bias in a statistical context. An estimate or measurement is said to be unbiased, if the estimator or measurement algorithm is *expected* to yield the 'true' value.

The measurements or estimates can still be noisy, i.e. *individual* shape measurements ϵ_i may have residual discrepancies with the true values ϵ (as a function of (ϵ^I, g), eq. 1.16). The *distribution* of estimates (realizations, measurements), however, should be 'centered', in some statistical sense, around that true value, for the measurement method to be called unbiased.

Usually, this definition of center is taken to be the mean or expected value, and the estimator (or measurement algorithm) is said to be mean-unbiased, if for an increasing number[14] of estimations, the mean estimate converges toward the value of interest of the underlying population. Note that we discuss here the distribution $P(\hat{\epsilon})$ of an estimator $\hat{\epsilon}$ of the ellipticity ϵ, that has its own distribution $P(\epsilon)$.

This unavoidable alteration of the sheared ellipticity distribution $P(\epsilon)$ means that the mean, the first moment $\langle \epsilon_i \rangle$, is no longer an unbiased tracer of g. This can partly be understood, by considering that the unbiasedness of $\langle \epsilon \rangle$ stems from the fact that the ellipticity distribution *before* the effect of gravitational shear is irrelevant, while the effect of noise, from whatever source other than intrinsic shape noise, is applied *after* the shear. Since that noise distribution will be (roughly) centered around $(0, 0)$, whether it be from noisy measurement or natural fluctuations in an isotropic universe, the observed distribution will be skewed low (see Fig. 1.6).
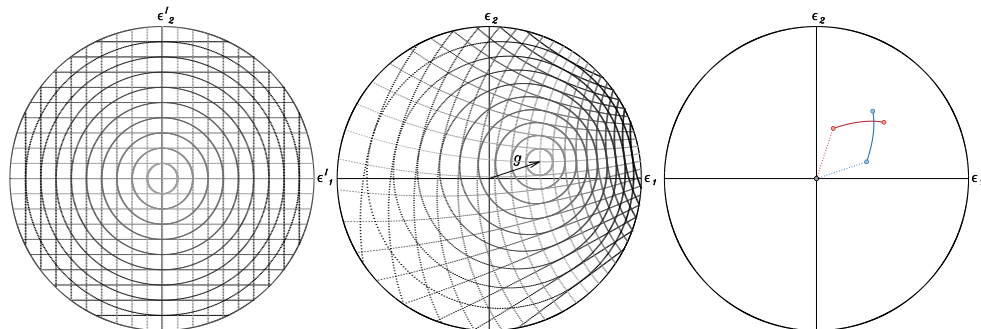

Figure 1.6: *Left and middle*: the non-linear mapping of ellipticities (with $|\epsilon \leq 1|$) by a reduced shear of $g = 0.33 + 0.11i$. *Right*: the noncommutative geometry of ϵ space. In blue, the resulting ellipticity $\epsilon_{a \to b}$ when applying a reduced shear g_b to an intrinsic ellipticity ϵ_a^I. In red, the resulting ellipticity $\epsilon_{b \to a}$ when applying a reduced shear g_a to an intrinsic ellipticity ϵ_b^I. Based on Smit et al. (2015).

At the same time, given that the intrinsic galaxy ellipticity distribution is confined to $|\epsilon^I| < 1$ and that any $g < 1$ will not cause a $\epsilon \geq 1$, the ellipticity 'space' we consider is a

---

[14]Since we technically take the limit to infinity, the central limit theorem justifies the use of the mean as measure of center of the *estimator* distribution, and for the use of the shorthand 'unbiased' for mean-unbiased.

highly non-Euclidean, bound but infinite[15] manifold (Bernstein & Jarvis 2002, see Fig. 1.6). One should therefore not speak of a linear difference $\epsilon_b - \epsilon_a$ between two ellipticity values ϵ_a and ϵ_b, but the *excess shearing* (defined by eq. 1.16) needed to transform ϵ_a into ϵ_b. Yet measurement pipelines such as the KSB and shapelets implementations used in chapters 2 and 3, allow for values $\epsilon \gg 1$, and the *lens*fit implementation in chapters 4 and 5 effectively truncates ellipticity space − again, even if the measurements are noisy but unbiased.

In chapters 4 and 5, we investigate the consequences for the inference of the underlying shear signal g.

Estimators and bias

Both observations (e.g. Lambas et al. 1992, Rodríguez & Padilla 2013, Smit & Kuijken 2018) and realistic theoretical models (see e.g. chapter 4) show that the intrinsic distribution of galaxy ellipticities is strongly non-Gaussian, but sharply peaked. For any realistic noise distribution, the shape of $P(\epsilon)$ is changed, but the location of this peak is still an unbiased tracer of the underlying shear. This is a powerful option, if we can accurately determine this location.

We considered several estimators as alternatives to the mean, less sensitive to outliers and/or more sensitive to a centrally peaked distribution. While the principle of the 'right' estimator for a distribution is an appealing one, in practice no estimator is generally unbiased, as noise distributions vary and are dependent on instrument and shape measurement pipeline.

1.2.4 Results and interpretation

And then, when one has a catalog of unbiased ellipticity measurements and an estimator that gives an unbiased (but still noisy) value for g, begins our interpretation of the reality we have partly inferred from the shadows on the wall.

To relate the lensing signal to the matter distribution, we rely on accurate estimates of e.g. the distances D involved (see Fig. 1.4) or the center of the structure of interest. But let's assume here for a moment, to regain some lightweightedness in this introduction, that such other necessities are of little consequence, i.e. the uncertainties and biases caused are of subdominant[16] effect: in our interpretation, we will then inevitably compare our results to an expectation, a preconceived model of the universe, in order to understand it. So, what are we actually looking at?

For instance, we have considered a single lensing event by a group or cluster of galaxies, where in practice, light rays travel to a constantly changing potential, due to the large scale structure of the universe. This leaves a statistical imprint, called cosmic shear, first detected by (Bacon et al. 2000, Van Waerbeke et al. 2000, Wittman et al. 2000). This field of gravitational lensing in itself provides a complement to cosmological parameter determinations derived from observations of e.g. the CMB (see e.g. Kilbinger 2015, for a review). For our study of lensing by groups or clusters of galaxies, this cosmic shear signal is an additional form of noise, i.e. we detect the signal from the cluster and the cosmic shear together (Hoekstra et al. 2011). In some cases, such as the supergroup observed in Smit et al. (2015, chapter

---

[15]By infinite, we mean that we can apply any $g < 1$ to any $\epsilon^I < 1$ an infinite, discrete amount of times, and still retain $\epsilon < 1$.

[16]But they are most certainly not, as will be discussed in chapters 2, 3, and 5.

2), there are even known matter overdensities in the background, that need to be taken into consideration.

In fact, background galaxy shapes can also be coherently affected by a mechanism known as intrinsic alignment (IA) that is not due to lensing at all. This is because background galaxies that reside in the same potential, have their intrinsic orientations influenced in the same way, for instance due to tidal forces or angular momentum (e.g. Crittenden et al. 2002).

This effect is then further confused by the lensing effect of such a potential on even more distant background galaxies, introducing a (negative) correlation between the intrinsic shapes of galaxies and the shear experienced by galaxies (e.g. Hirata & Seljak 2004).

And, coming full circle to the start of this introduction, we study the shapes of the components of background galaxies that are *visible* to us, even though the vast majority of matter is dark and could be misaligned with the visible shapes. For our work, these effects are assumed to average out, only slightly increasing uncertainties, but we mention them here in reflection on the bigger picture.

This thesis is therefore not a road map to climb out of the cave. It does intend to provide a possible foothold, when contemplating that long climb.

1.3   Thesis outline

This thesis covers four studies into weak gravitational lensing, consisting of a theoretical consideration of the statistics of weak shear inference, and three separate studies of weak lensing by galaxy groups or clusters, exploring various aspects that obscure direct observations of gravitational shear.

1.3.1   Mass distribution in an assembling super galaxy group at $z = 0.37$

Chapter 2 is based on Smit et al. (2015) and presents a weak gravitational lensing analysis of supergroup SG1120−1202 (Gonzalez et al. 2005), consisting of four distinct X-ray-luminous groups that will merge to form a cluster comparable in mass to Coma at $z = 0$. This supergroup was discovered in the Las Campanas Distant Cluster Survey (Gonzalez et al. 2001) and has been studied in a series of papers (Gonzalez et al. 2005, Tran et al. 2008, 2009, Kautsch et al. 2008, Freeland et al. 2011, Just et al. 2011, Smit et al. 2015, Monroe et al. 2017).

The member groups lie within a projected separation of 1 to 4 Mpc and within $\Delta v = 550$ km s^{-1}, which is comparable to distances in the bullet cluster system (Tucker et al. 1995, Markevitch et al. 2002, Clowe et al. 2004), and as such, form a unique protocluster to study the matter distribution in a coalescing system.

We studied the weak gravitational distortion of background galaxy images by the matter distribution in the supergroup with high-resolution HST/ACS imaging. To robustly assess the systematic image distortions and artifacts present in these images, we used the shape measurement methodology for HST/ACS imaging outlined in (Schrabback et al. 2010), based on KSB+ (Erben et al. 2001).

We compared the reconstructed projected density field with the distribution of galaxies and hot X-ray emitting gas in the system and show that the projected mass distribution closely follows the locations of the X-ray peaks and associated brightest group galaxies. Since the

groups show no visible signs of interaction, our findings support the hypothesis that we observe the groups before they merge into a cluster.

We derived halo parameters for the individual density peaks, finding velocity dispersions between 355^{+55}_{-70} and 530^{+45}_{-55} km s^{-1} and masses between $0.8^{+0.4}_{-0.3} \times 10^{14}$ and $1.6^{+0.5}_{-0.4} \times 10^{14}$ h^{-1} $M_\odot$, consistent with independent measurements.

1.3.2 Weak lensing by very low redshift groups: analysis of systematics and robust shape measurements

In **chapter 3**, we studied the weak gravitational lensing signal from 79 low redshift groups ($0.05 < z < 0.0585$) from the 2dF Percolation-Inferred Galaxy Group catalog (2PIGG, Eke et al. 2004), based on the Two-degree-Field Galaxy Redshift Survey (2dFGRS, Colless et al. 2001), and observed with the Wide Field Imager (WFI) as part of the Zürich Environmental Survey (ZENS, Carollo et al. 2013). These groups cover two orders or magnitude in mass, with velocity dispersion $38 \lesssim \sigma \lesssim 691$ km s^{-1}, inferred mass $10^{12} \lesssim M \lesssim 10^{14}$ h^{-1} $M_\odot$, and $b_{\rm J}$ luminosity $1.1 \times 10^{10} \lesssim L \lesssim 5.9 \times 10^{11}$ h^{-2} $L_\odot$. The aims of this work were twofold.

Firstly, these groups covered a mass range that had not been studied extensively yet at the time of this research, filling a niche in the mass spectrum. Most weak lensing studies had been into large scales, up to those of clusters and superclusters, and into small scales, the lensing by individual galaxies. On intermediate scales, there were results in the high mass group regime (see e.g. Mandelbaum et al. 2006, Leauthaud et al. 2010) and Hoekstra et al. (2001) reported the first measurements of light galaxy groups in the CNOC2.

Secondly, this research could be a suitable pathfinder for the Kilo-Degree Survey (de Jong et al. 2013), which has an extensive overlap with the 2dFGRS and this sample. Given the low redshift and low median mass of these groups, which translate to a weak gravitational lensing signal, this work focused extensively on understanding possible systematics in wide-field imaging data, shape measurements methods and the statistical effect of outliers.

And important part of the analysis of systematics was estimating the effect of stacking of exposures on PSF correction and shape measurements, comparing the shapes of stars and sources detected in varying number of exposures and sources detected on multiple parts of the CCD array, due to being present in overlapping fields of view.

To asses the robustness of shape measurements, we compared two different pipelines, namely KSB+ (Erben et al. 2001), based on surface brightness moments, and shapelets (Kuijken 2006), considered a model fitting method. The results were statistically consistent.

We analyzed the effect of outliers in shape measurements of the inference of the weak shear signal, by comparing the commonly used weighted mean of a sample of ellipticities to the estimated obtained by convex hull peeling (CHP). The results were comparable in this respect as well.

Finally, we derived estimates for the velocity dispersion by fitting the lens profile for a singular isothermal sphere (SIS), and estimates for the mass and concentration of the groups, by fitting a Navarro, Frenk & White profile (NFW, Navarro et al. 1996), in good agreement with the dynamical estimates from 2PIGG.

1.3.3 Optimal statistics for weak shear analyses

Chapter 4 is based on Smit & Kuijken (2018), the first of a set of papers (with chapter

5 describing the second), and continues the analysis of optimal methods for inferring the gravitational shear from a sample of measured ellipticities of background galaxies.

This way of determining the shear signal is fundamentally limited by the intrinsic distribution of shapes that galaxies exhibit. It is well known that the distribution of galaxy ellipticities is non-Gaussian (e.g. Lambas et al. 1992, Rodríguez & Padilla 2013), and traditional estimation methods, explicitly or implicitly assuming Gaussianity, lead to noise biases (e.g. Kacprzak et al. 2012, Melchior & Viola 2012), possibly of the order of a few percent. This makes them comparable or even dominant to other sources of uncertainty in the process, such as biases in shape measurement, uncertainty in the lensing geometry introduced by photometric redshift probability distributions, or selection biases.

An optimal estimator is, from a principled point of view, more objective and better suited than corrections to an approach that is known to mismatch the sample distribution. In this work, we refine our method of CHP and complement that method and the canonical weighted mean (or weighted least squares or L^2 estimator) by the least absolute deviations (LAD or L^1) estimator and the biweight estimator (Beaton & Tukey 1974). We also allowed for a range of possible ellipticity distributions, comparing a Gaussian distribution with a flat axis ratio distribution, an ellipticity distribution from projected ellipsoids and the ellipticity distribution in the CFHTLenS shear catalog(Heymans et al. 2012b).

We analyzed the biases, relative efficiencies and robustness of these estimators. We conclude that the LAD estimator is the most robust when applied to our simulations, reducing noise bias by more than $\sim 30\%$, while increasing efficiency by a factor of 5 in the ideal case, and a factor of 1.2 when applied to CFHTLenS data.

We applied these methods to fitting of Fourier modes to the pattern of ellipticities in a simulated image, as a proof of concept.

1.3.4   AMICO galaxy clusters in KiDS-DR3: the impact of estimator statistics on the luminosity-mass scaling relation

In **chapter 5**, based on Smit et al. (2021), we apply the findings of the analysis described in chapter 4 on data from the third KiDS data release (KiDS-450, de Jong et al. 2017). We use the shape measurements of background sources around 6925 clusters found in KiDS-450 using the Adaptive Matched Identifier of Clustered Objects (AMICO, Bellagamba et al. 2011, Radovich et al. 2017, Bellagamba et al. 2018) and compare the results obtained with the weighted LAD and mean estimators.

The high signal-to-noise ratio of the shear signal allows us to study the scaling relation between the r-band cluster luminosity L_{200}, and the derived lensing mass M_{200}. We show the results of the scaling relations derived in 13 bins in L_{200}, with a tightly constrained power law slope of $\sim 1.24 \pm 0.08$.

We observe a small, but significant relative bias of a few percent in the results of the two regression methods, which is in excellent agreement with our findings in chapter 4. The efficiency of LAD is at least that of the weighted mean, relatively increasing with higher signal-to-noise shape measurements, a further confirmation of our previous results. As such, LAD regression provides a robust consistency check for shear inference, which has been and still remains a major investment in the field of weak lensing, while increased computation times remain feasible.